

Production of Jets before Neutron Star Mergers

PRAVEEN SHARMA,¹ MAXIM LYUTIKOV,² SLAVA G. TURYSHEV,³ AND MAXIM V. BARKOV⁴

¹*Department of Physics & Optical Engineering, Rose-Hulman Institute of Technology, 5500 Wabash Ave, Terre Haute, IN 47803, USA*

²*Department of Physics, Purdue University, 525 Northwestern Avenue, West Lafayette, IN 47907, USA*

³*Jet Propulsion Laboratory, California Institute of Technology, 4800 Oak Grove Drive, Pasadena, CA 91109, USA*

⁴*Institute of Astronomy, Russian Academy of Sciences, Moscow, 119017, Russian Federation*

Abstract

We demonstrate that magnetospheric interactions between merging neutron stars (NSs) generate dual-jetted current outflows, analogous to the Alfvén wings observed during planetary interactions in the Solar System. Using 3D relativistic MHD simulations, we model the interaction as a conducting sphere moving through a highly magnetized plasma of the companion’s magnetosphere. Unusually, the interaction operates in a regime that is relativistic yet sub-Alfvénic. Electromagnetic draping amplifies magnetic fields in a narrow layer near the stellar surface, leading to the generation of electric currents along the local magnetic field. The generation of beamed outflows enhances instantaneous power of the pulsar-like radio and high energy emission, produces spin/orbital modulations, and is likely to lead to observable precursor emission preceding the main gravitational wave event.

Keywords: Neutron stars (1108) — Magnetohydrodynamics (1964) — Plasma astrophysics (1261) — Compact binary stars (283)

1. INTRODUCTION

Neutron star mergers represent key targets for Multi-messenger astronomy, serving as sources of gravitational waves and potential progenitors of short gamma-ray bursts (GRBs). Detecting electromagnetic precursors to such mergers would provide valuable early warnings and insights into merger physics. The most promising mechanism for generating such precursor emission is the electromagnetic interaction between merging compact objects through inductive electric fields created by relative motion within their common magnetosphere (Hansen & Lyutikov 2001; Lai 2012; Metzger & Berger 2012; Most & Philippov 2020; Mahlmann & Beloborodov 2024; Lyutikov 2024).

Since merger timescales are typically long (Portegies Zwart & Spera 1996), by the time of the merger, the neutron stars are likely to have spun down and become electromagnetically “dead” – not actively producing pairs in the classical pulsar manner (Goldreich & Julian 1969). Even fast merger channels are long enough for typical pulsars to switch off (Andrews et al. 2020). However, as orbital inspiral progresses, the magnetospheres can be reactivated through their relative orbital motion (Lyutikov 2019, 2024).

Both single magnetized (1M-DNS) and double-magnetized (2M-DNS) cases are possible (Lyutikov 2019). Our work focuses on the 1M-DNS case, where an unmagnetized, highly conducting neutron star moves through the magnetic field of its companion. This scenario shares qualitative similarities with planetary magnetosphere interactions (Goldreich & Lynden-Bell 1969), but exhibits crucial differences due to the extreme conductivity of neutron stars and the possibility of relativistic velocities during late-stage inspiral.

Magnetic interaction of merging neutron stars is expected to proceed in an unusual (by space physics) regime: (i) plasma is expected to be highly magnetized, with $\sigma = (\omega_B/\omega_p)^2 \geq 1$ (and, correspondingly $\beta \ll 1$); (ii) interaction velocities may be mildly relativistic $\sim c$, as near merger the Keplerian velocity is close to the speed of light. This unusual regime is the goal of the present study. (For example, the interaction may be in a regime of relativistic but sub-Alfvénic.)

The key points of the present work are: (i) motion of a conducting star through magnetosphere of a companion creates an EMF, and can possibly lead to The generation of observable emission; (ii) resulting current structure resembles Alfvén wings observed planetary interactions; the resulting emission pattern is then expected to be anisotropic, leading to higher peak fluxes and orbital or spin modulations.

The rest of the paper is organized as follows: § 2 describes non-relativistic case (planetary Alfvén wings), theoretical background and expectations for the relativistic regimes; § 3 details the numerical setup; § 4 presents simulation results for non-relativistic flows spanning sub-Alfvénic to super-Alfvénic regimes; § 5 presents results for mildly relativistic flows and compares them with classical predictions; and § 6 provides discussion and conclusions regarding the implications for neutron star merger precursor emission.

2. THEORETICAL BACKGROUND

2.1. *Alfvén wings in planetary interactions*

The interaction of conducting bodies with magnetized plasma is well established in space plasma environments and displays markedly different behavior depending on both conductivity and flow regime. A particular feature of interaction is the formation of so-called Alfvén wings.

Alfvén wings are routinely realized in planetary and satellite environments whenever a conducting (or effectively conducting) obstacle is embedded in a sub-Alfvénic magnetized flow ($\mathcal{M}_A < 1$). In this regime, the response to the obstacle is not mediated by a detached bow shock but by stationary Alfvénic characteristics, which allow stresses and currents to propagate both upstream and downstream along the ambient magnetic field (Gurevich 1962; Drell et al. 1965; Neubauer 1980; Saur et al. 2013). In the obstacle frame, the two Alfvén wings are aligned with the characteristic directions

$$\mathbf{u}_\pm \equiv \mathbf{v}_0 \pm v_A \hat{\mathbf{b}}, \quad (1)$$

where $\hat{\mathbf{b}} \equiv \mathbf{B}_0/|\mathbf{B}_0|$ and v_A is the Alfvén speed. For the commonly used geometry $\mathbf{v}_0 \perp \mathbf{B}_0$, the wing inclination relative to \mathbf{B}_0 satisfies $\tan \theta_A \simeq \mathcal{M}_A$, where \mathcal{M}_A is upstream Alfvén Mach number.

In the solar system, Alfvén wing structures are observed when a conducting obstacle is embedded in a sub-Alfvénic flow. For example, Earth's magnetosphere has been observed forming Alfvén wing connected current systems in the solar wind (Gurram et al. 2025). Similar processes occur at the Moon, although its weak conductivity and lack of an intrinsic magnetic field lead to plasma wake formation rather than stable wings (Chané et al. 2012; Zhang et al. 2016). The most direct analogues for strongly conducting bodies are Jupiter's moons. Io's volcanically sustained ionosphere and Ganymede's intrinsic magnetic field each generate coherent Alfvén wings and associated field-aligned current systems (Vernisse et al. 2017; Neubauer 1999; Kopp & Ip 2002), which are observable through auroral and radio signatures (Mottez & Zarka 2014; Caruso et al. 2024). Extensions of Alfvén wing theory to relativistic flows have been explored in the context of pulsar winds and orbiting bodies by Mottez & Heyvaerts (2011), demonstrating that strong currents can be driven even when the body is immersed in a relativistic plasma flow. These examples clearly demonstrate that conducting obstacles in magnetized plasma flows produce electromagnetic structures that efficiently channel energy and can be detected observationally.

Quantitatively, the planetary Alfvén -wing interaction can be expressed as an effective electrodynamic circuit in which the moving obstacle acts as a unipolar generator. For an obstacle of radius R_p embedded in a magnetized flow with $\mathbf{v}_0 \perp \mathbf{B}_0$, the motional field is $\mathbf{E}_0 \simeq \mathbf{v}_0 \mathbf{B}_0$, yielding an induced electromotive force $\Delta\Phi \simeq 2R_p \mathbf{E}_0 \simeq 2R_p v_0 B_0$ (Drell et al. 1965; Goldreich & Lynden-Bell 1969; Neubauer 1980). The associated field-aligned current is limited by the Alfvén -wave conductance $\Sigma_A \simeq (\mu_0 v_A)^{-1}$ (equivalently, impedance $Z_A \simeq \mu_0 v_A$), so in the high-conductance limit one expects $I \sim 4R_p \mathbf{E}_0 \Sigma_A$ and a total electromagnetic power extraction $P_{AW} \sim I \Delta\Phi \sim 8R_p^2 \mathbf{E}_0^2 \Sigma_A$ transported along the two wings. For the Io-Jupiter interaction, inserting representative values ($R_p \simeq 1.82 \times 10^6$ m, $v_0 \sim 5 \times 10^4$ – 7×10^4 m s $^{-1}$, $B_0 \sim 10^{-6}$ – 2×10^{-6} T, $v_A \sim 10^5$ – 3×10^5 m s $^{-1}$) gives $\Delta\Phi \sim \text{few} \times 10^5$ V, $I \sim \text{few} \times 10^6$ A, and $P_{AW} \sim 10^{12}$ W, consistent with in-situ magnetic perturbations and remote auroral footprint constraints (Kivelson et al. 1996; Clarke et al. 1996, 2002; Chust et al. 2005).

These planetary observations motivate two points directly relevant to the present neutron-star problem. First, they show that Alfvén wings can remain coherent over distances vastly exceeding the obstacle size, so long as $\mathcal{M}_A < 1$ and dissipation does not destroy the field-aligned current channels (Neubauer 1980; Clarke et al. 2002). Second, they demonstrate that the most readily observable signatures are frequently indirect: auroral footprints, lead angles, and radio emission reflect the Poynting flux and current carried by the wings rather than the near-body fields alone. Our simulations are designed to isolate the underlying MHD wing morphology and current topology, enabling a controlled comparison between the classical planetary regime and the neutron-star limit where the conductivity is effectively infinite and relativistic effects become important.

While in the above discussion, we used SI circuit notation (μ_0, Ω) for comparison with space-physics literature, all simulation variables and plasma parameters elsewhere are in CGS or code units.

2.2. The unipolar inductor model

Neutron stars represent the extreme limit of this physics. Their matter composition renders them effectively perfect conductors ($\sigma \rightarrow \infty$), enforcing a boundary condition that expels magnetic flux from the stellar interior. As a result, magnetic field lines drape tightly around the surface, forming thin current layers whose structure depends on the flow velocity regime. These layers primarily amplify magnetic fields through compression and can develop enhanced current concentrations, though the conditions for efficient particle acceleration and radiation remain to be explored with kinetic-scale simulations.

In a relativistic regime, the basic estimate of electromagnetic power from a relativistic unipolar inductor (Blandford 2002) is

$$L \sim \frac{c}{4\pi} (\Delta\Phi)^2, \quad (2)$$

where $\Delta\Phi \sim vBD$ is the EMF drop for a conductor of size D moving at speed $v = \beta c$ in a magnetic field B .

For a singly-magnetized case (1M-DNS) (Lyutikov 2019), the power scales as:

$$L_{\text{1M-DNS}} \sim \frac{B_{\text{NS}}^2 G M_{\text{NS}} R_{\text{NS}}^8}{c r^7} \approx 3 \times 10^{43} t^{-7/4} B_{13}^2 \text{ erg s}^{-1} \quad (3)$$

The power in the double-magnetized (2M-DNS) case, L_2 , is larger by a factor of $\approx (r/R_{\text{NS}})^2$. This enhancement arises because the magnetospheric interaction in the 2M-DNS scenario occurs on the scale of the orbit, whereas in the 1M-DNS case, it is confined to the scale of the companion NS.

The estimates in Eq. (3), normalized to a relatively large surface magnetic field of 10^{13} G, highlight a potential issue: the overall expected power is not particularly large. If emitted isotropically, it will be missed by high-energy all-sky X-ray monitors.

We demonstrate: (i) the emission is likely to be beamed; and (ii) one might expect the generation of coherent radio emission, *a la* pulsar-style. If a significant fraction of the energy is emitted in coherent radio, the expected peak flux density is given in Jansky (Hansen & Lyutikov 2001; Lyutikov 2019; Cooper et al. 2023). The radio signal will also experience a dispersive delay of

$$\Delta t \simeq 14 \text{ sec} \left(\frac{\nu}{1 \text{ GHz}} \right)^{-2} \left(\frac{d}{200 \text{ pc}} \right), \quad (4)$$

where ν is the observing frequency, d is the source distance in parsecs, and Δt is the dispersive delay (Pshirkov & Postnov 2010; Tian et al. 2023).

3. NUMERICAL SIMULATIONS

We conduct three-dimensional magnetohydrodynamics (MHD) simulations using the `PLUTO` code version 4.3 (Mignone et al. 2007) to investigate magnetic draping around solid obstacles in both classical non-relativistic and relativistic regimes. The code solves the full set of ideal (R)MHD equations using high-resolution shock-capturing schemes optimized for curvilinear coordinate systems. Our focus remains on magnetohydrodynamic processes, neglecting external and self-gravity effects, as electromagnetic interactions dominate the dynamics in the regimes of interest.

3.1. Code Setup

We model the neutron star as a dense, non-rotating, perfectly conducting sphere of radius R_{\star} embedded in an ambient magnetized plasma. The star is assumed to be unmagnetized and highly conducting, and interacts with the magnetic field of a companion star. We work in the star's rest frame so that the neutron star remains fixed in space. Far from the sphere ($r \gg R_{\star}$), the plasma flows with velocity $\mathbf{v} = -v_0 \hat{\mathbf{x}}$ from right (upstream) to left (downstream).

Non-relativistic simulations use a Courant-Friedrichs-Lowy (CFL) number of 0.4 and the Harten-Lax-van Leer (HLL) Riemann solver. The divergence constraint $\nabla \cdot \mathbf{B} = 0$ was enforced using `PLUTO`'s eight-wave formulation (Powell 1994; Powell et al. 1999). We monitored the dimensionless volume-averaged normalized divergence error $\Delta x \langle |\nabla \cdot \mathbf{B}| \rangle / \langle |\mathbf{B}| \rangle$. This metric remained below 10^{-3} , indicating good divergence control.

Relativistic runs adopt CFL=0.25, the HLLD solver (Mignone et al. 2009), and an adiabatic index $\gamma = 4/3$. The domain uses a stretched grid with $N_x = N_y = N_z = 170$, giving a minimum cell size $\Delta x \sim 0.04 R_{\star}$. Divergence is controlled through hyperbolic cleaning (Dedner et al. 2002). The divergence constraint was handled through the

hyperbolic divergence cleaning method (Dedner et al. 2002). The normalized divergence error remained below 10^{-3} with the characteristic cell.

The stretched grid concentrates resolution near the stellar surface. For the fiducial relativistic runs ($N=170$), $\Delta x_{\min} \approx 0.034 R_\star$, marginally resolving the predicted draping layer thickness $\delta_r \sim (v_0/c)^2 R_\star \sim 0.04 R_\star$. Convergence studies (Appendix A.3) confirm that integrated quantities, such as wing current and magnetic amplification, are robust across resolutions $N = 113$ – 190 .

All runs employ PLUTO with second-order Runge-Kutta (RK2) time-stepping. A detailed description of the numerical setup, boundary conditions, along with the discussion of divergence cleaning and convergence, is discussed in detail in the Appendices A, B.

3.2. Interaction parameters

To characterize the interaction of magnetized plasmas with obstacles, we now discuss key dimensionless parameters that govern the flow. The primary parameter across different runs is the upstream Alfvénic Mach number $\mathcal{M}_A = \frac{v_0}{v_{A0}}$ where $v_{A0} = \sqrt{B_0^2/\rho_0}$ is the Alfvén speed in the ambient medium far away from the central obstacle.

Another important parameter is the plasma beta $\beta = \frac{p_{\text{thermal}}}{p_{\text{mag}}}$ which measures the relative importance of thermal plasma pressure to magnetic pressure. Since neutron star magnetospheres are typically magnetically dominated, we focus on low β regimes ($0.01 \leq \beta \leq 0.02$) in our non-relativistic runs. Our relativistic runs explore slightly higher values ($\beta \approx 0.16$ – 0.80), chosen to ensure numerical stability in the relativistic MHD regime.

For relativistic flows, these parameters must be evaluated using comoving-frame quantities. Primed variables denote the plasma rest frame. We introduce the magnetization parameter

$$\sigma' \equiv \frac{2p'_{\text{mag}}}{\rho'_0 c^2} \quad (5)$$

which compares magnetic to rest-mass energy density: $\sigma' \ll 1$ corresponds to matter-dominated flows, while $\sigma' \gg 1$ corresponds to magnetically dominated flows.

The characteristic wave speeds in relativistic MHD (see Eqs. 38–46 in (Gedalin 1993); also Lyutikov & Hadden 2012) evaluated in the co-moving frame are given by

$$\begin{aligned} v'_A &= c \sqrt{\frac{\sigma'}{h' + \sigma'}}, \\ v'_s &= \sqrt{\frac{\gamma p}{\rho' h'}}, \\ v'_f &= \sqrt{v'_A^2 + v'_s^2 - \frac{v'_A^2 v'_s^2}{c^2}} \end{aligned} \quad (6)$$

where $h' \equiv \frac{\epsilon' + p}{\rho' c^2}$ is the specific enthalpy, with ϵ' the internal energy density and ρ' the rest-mass density in the plasma rest frame. For an ideal-gas equation of state, $\epsilon' = \rho' c^2 + \frac{p}{(\gamma-1)}$ (Mattia et al. 2023), with γ being the adiabatic index.

The relativistic Alfvén Mach number is defined using

$$\mathcal{M}_A = \frac{\Gamma v_0}{\Gamma_A v'_A}, \quad \Gamma_A = \left(1 - \frac{v'_A^2}{c^2}\right)^{-1/2} \quad (7)$$

which can also be written as

$$\mathcal{M}_A = \frac{\Gamma v_0}{c} \sqrt{\frac{h'}{\sigma'}}. \quad (8)$$

with analogous definitions for \mathcal{M}_s and \mathcal{M}_f .

A simplified non-relativistic analogy $\mathcal{M}_A \approx v_0/v'_A$ is sometimes used in the literature, but it neglects the Lorentz transformation properties of both the bulk flow and the characteristic wave speeds. The definition in Eq. 7 is fully relativistic and frame-invariant (cf. Eq. 37 of Zanotti et al. (2015); Chow et al. (2023)).

3.3. Simulation Runs

Using the dimensionless parameters defined above, we construct a set of representative models spanning sub-Alfvénic and super-Alfvénic regimes in both classical and relativistic limits. The principal runs discussed in this work are summarized in Table 1.

Non-relativistic runs (A-series): The fiducial sub-Alfvénic run A1 ($\beta = 0.01$, $\mathcal{M}_A = 0.08$) represents the strongly magnetized plasma conditions characteristic of certain planetary magnetospheres and of regions immediately surrounding neutron stars. Runs A2 ($\mathcal{M}_A = 0.63$) and A3 ($\mathcal{M}_A = 2.19$) probe the moderately sub-Alfvénic and trans-Alfvénic regimes.

Relativistic runs (B-series): The relativistic runs span the sub-Alfvénic to trans-Alfvénic regimes. The fiducial run B1 ($\Gamma_0 = 1.05$, $\mathcal{M}_A \approx 0.21$, $\beta = 0.40$) explores the mildly relativistic sub-Alfvénic flow. Run B2 ($\Gamma_0 = 1.15$, $\mathcal{M}_A \approx 0.65$, $\beta = 0.40$) represents the moderately sub-Alfvénic regime. Run B3 ($\mathcal{M}_A \approx 1.91$, $\beta = 0.80$) approaches trans-Alfvénic conditions. Simulations at substantially lower β (values similar to the non-relativistic runs) become unstable in the relativistic module, owing to the increased stiffness of the RMHD system and associated difficulties in primitive-variable recovery.

Run	β	\mathcal{M}_A	\mathcal{M}_f
A1	0.01	0.08	0.073
A2	0.01	0.63	0.61
A3	0.02	2.19	1.96

(a) Non-relativistic (A-series)

Run	$v_0/c (\Gamma_0)$	β	\mathcal{M}_A	\mathcal{M}_f
B1	0.30 (1.05)	0.16	0.21	0.17
B2	0.50 (1.15)	0.40	0.65	0.47
B3	0.50 (1.15)	0.80	1.91	1.42

(b) Relativistic (B-series)

Table 1. Simulation parameters for the selected runs discussed in this work. Columns list the plasma β , and Alfvénic (\mathcal{M}_A) and fast magnetosonic (\mathcal{M}_f) Mach numbers. Relativistic runs include the Lorentz factor Γ_0 , with velocities expressed in terms of the speed of light, with the corresponding Lorentz factors shown in brackets.

The characteristic timescale of the interaction is the Alfvén crossing time,

$$\tau_A \equiv \frac{R_\star}{v_A}, \quad (9)$$

and all simulations are evolved for several τ_A to ensure the development of steady-state structures.

4. NON-RELATIVISTIC FLOW

Although our primary interest is in the relativistic MHD runs, we first analyze a set of non-relativistic simulations to establish a baseline for interpreting the relativistic results. By systematically varying the Alfvén Mach number (\mathcal{M}_A), we characterize how the global morphology transitions from magnetically controlled to shock-dominated flow.

We begin with the classical sub-Alfvénic limit and then consider the trans-Alfvénic regime, before turning to the relativistic cases in §5.

4.1. Sub-Alfvénic Regime

We first examine the fiducial strongly magnetized and strongly sub-Alfvénic case (Run A1), which provides a reference for magnetically dominated interactions. Fig. 1(a) shows 2D slices of the normalized flow velocity across two physically relevant planes. The flow remains largely symmetric about the upstream axis and closely follows the imposed background state far from the star. As the plasma approaches the conducting sphere, it decelerates and is smoothly redirected along magnetic field lines, producing coherent Alfvén wings at an angle $\theta_A \simeq \tan^{-1} \mathcal{M}_A \approx 5^\circ$. These appear as extended regions of reduced velocity and gentle deflection in the meridional plane, while perturbations perpendicular to the flow remain small.

The density and ram-pressure distributions reflect this magnetic channeling (Fig. 1b–c). In the equatorial (xy) plane, the upstream plasma remains mostly undisturbed, except for an underdense ring very close to the star. Immediately downstream, a dense lobe forms behind the star, followed by a sharp transition to an extended low-density wake. In the xz plane, a similar dense lobe appears immediately behind the star, but the downstream structure extends farther,

forming a broad V-shaped under-dense region. High-density regions surrounding this wedge form wing-like structures, with these features corresponding to Alfvén wings and their associated compression zones. Regions of high density coinciding with low ram pressure correspond to stagnation near the conducting surface, where the velocity approaches zero.

Magnetic pressure maps further highlight this behavior. We first present the 3D isocontour plots of the magnetic pressure distribution in Fig. 2, followed by 2D slices in Fig. 1(d). In the xy plane, we observe a thin ring-like structure with enhanced magnetic pressure surrounding the obstacle. In the xz plane, magnetic pressure reaches local minima near the poles, while roughly symmetric peaks appear in the equatorial regions on either side of the star. The downstream wake shows strong magnetic pressure depletion. This organized topology is consistent with a sub-Alfvénic flow unable to penetrate the stellar magnetosphere. The fast magnetosonic Mach number remains globally sub-fast ($\mathcal{M}_f \lesssim 1$), with only small localized super-fast patches near the flanks and poles. Overall, this run exhibits the expected picture of a magnetically controlled interaction characterized by coherent wings, modest compression, and smooth flow deflection.

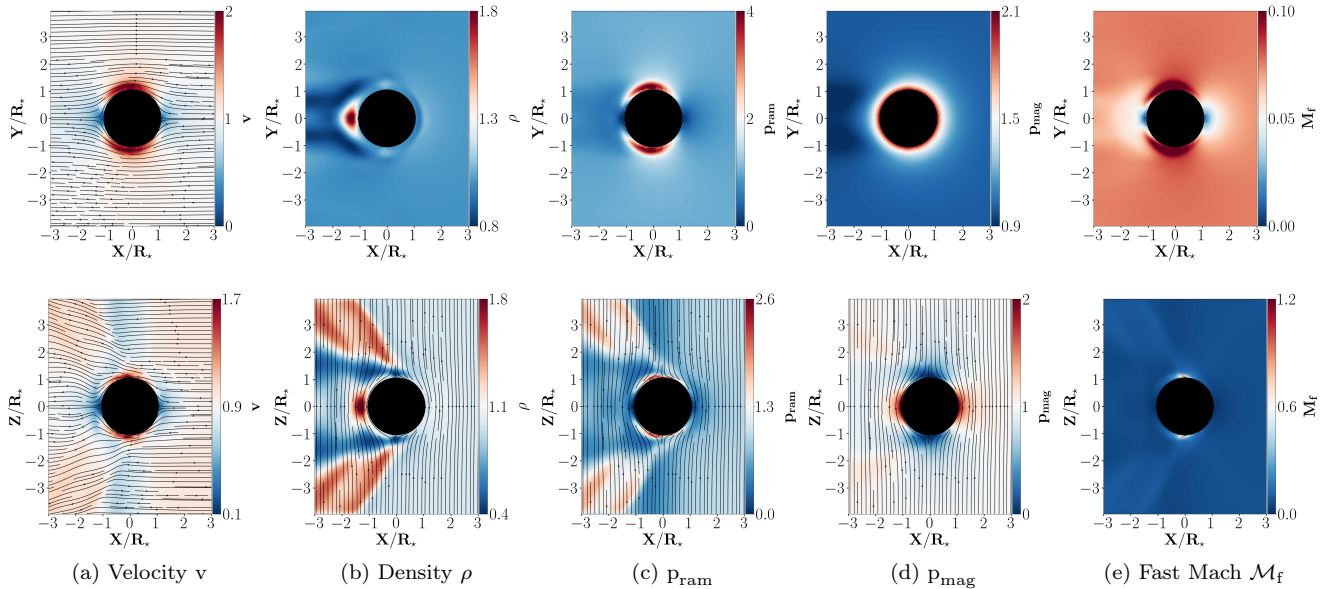


Figure 1. Non-relativistic Sub-Alfvénic run A1. Top row: xy -plane slices of flow velocity (v), density (ρ), ram pressure (p_{ram}), and fast magnetosonic Mach number (\mathcal{M}_f). Bottom row: corresponding xz -plane slices. All quantities, except \mathcal{M}_f , are normalized by the upstream values. Velocity Streamlines and magnetic field lines are overlaid where applicable. The green contour in fast Mach plots marks the boundary $\mathcal{M}_f = 1$.

Current Systems and Dissipative Regions

The sub-Alfvénic interaction establishes a set of coupled current systems linking the stellar surface to the surrounding flow. Surface currents form along the conducting boundary to enforce flux exclusion and cancel tangential electric fields, while field-aligned currents are diverted into a pair of symmetric Alfvén wings that carry electromagnetic energy away from the obstacle. Fig. 3 illustrates this topology using the sub-Alfvénic run A1c ($\mathcal{M}_A = 0.26$), where the larger opening angle ($\theta_A \simeq \tan^{-1}(\mathcal{M}_A) \approx 15^\circ$) makes the wing structure visually prominent. We are still in the deeply sub-Alfvénic regime, so the overall physics remains consistent with run A1. The background magnetic field \mathbf{B}_0 is shown by vertical black arrows, whereas the inflow plasma velocity is represented by the dark teal dashed arrows.

Iso-surfaces of $|\mathbf{J}|$ reveal two collimated current channels extending from the stellar surface at the expected Alfvén angle. Streamlines colored by J_z show that these currents are predominantly field-aligned and flow in opposite directions above and below the equatorial plane, forming the characteristic bipolar Alfvén wing system. Enhanced current density immediately surrounding the star marks the thin draping layer where magnetic flux is compressed around the conducting surface. The overall morphology is consistent with classical Alfvén wing interactions observed in planetary magnetospheres (Bagenal & Dols 2020; Vernisse et al. 2017).

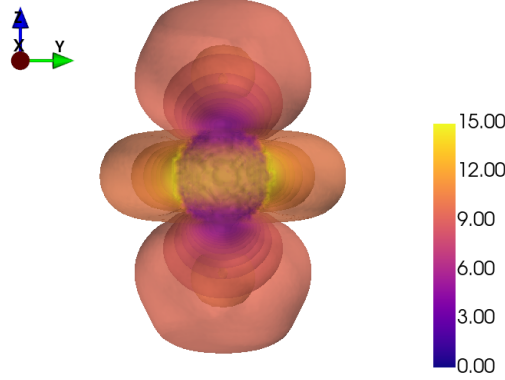


Figure 2. Non-relativistic Sub-Alfvénic run A1. 3D contour plot of the magnetic pressure $B^2/8\pi$ at the steady state viewed along the x-axis.

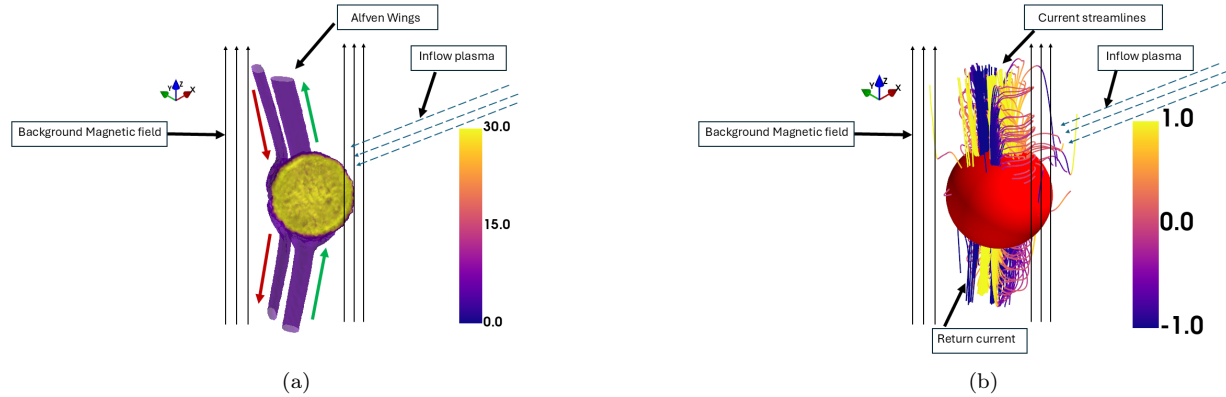


Figure 3. Alfvén wing structure in illustrative run A1c. (a) Isosurface of current density magnitude $|J|$ showing bipolar field-aligned current channel (purple) extending from the neutron star surface. The green and red arrows on the wings indicate upward ($+z$) and downward ($-z$) directed currents, respectively, forming the bipolar Alfvén wing current system. (b) Current streamlines colored by J_z component, revealing the field-aligned nature of the currents. Both panels show arrows indicating ambient magnetic field \mathbf{B}_0 (black) and flow velocity \mathbf{v}_0 (dark teal).

Having established the Alfvén wing morphology with the more visually prominent case A1c, we now return to our highly sub-Alfvénic fiducial run A1. The same current system persists, but with more tightly collimated wings ($\theta_A \approx 5^\circ$). Viewed along the $+z$ direction (left), an upstream–downstream asymmetry is evident. Upstream, currents form organized loops from the magnetic field bending around the star’s surface. Downstream ($x < 0$), the wake contains current channels that extend along field lines, representing sites of potential electromagnetic emission. In the lateral regions ($\pm y$ directions), current streamlines circulate in opposite senses above and below the equator (clockwise vs. counterclockwise), providing closure paths that connect the surface currents to the Alfvén wing channels.

We emphasize that these field-aligned current channels represent Alfvén -wing structures characteristic of sub-Alfvénic magnetospheric interactions, rather than mass-loaded relativistic jets. The ideal MHD framework employed here does not capture jet formation mechanisms such as particle acceleration or radiative cooling that would be required to model astrophysical jets in the traditional sense.

Two-dimensional slices of the parallel current component (Fig. 5) further highlight this structure. The $x = 0$ plane shows a clear bipolar pattern aligned with the background magnetic field and confined near the stellar surface by the draping layer, whereas in the $y = 0.5$ plane, the current distribution exhibits an upstream–downstream asymmetry, upstream currents remain weak and diffuse, whereas downstream currents form well-organized channels within the wake.

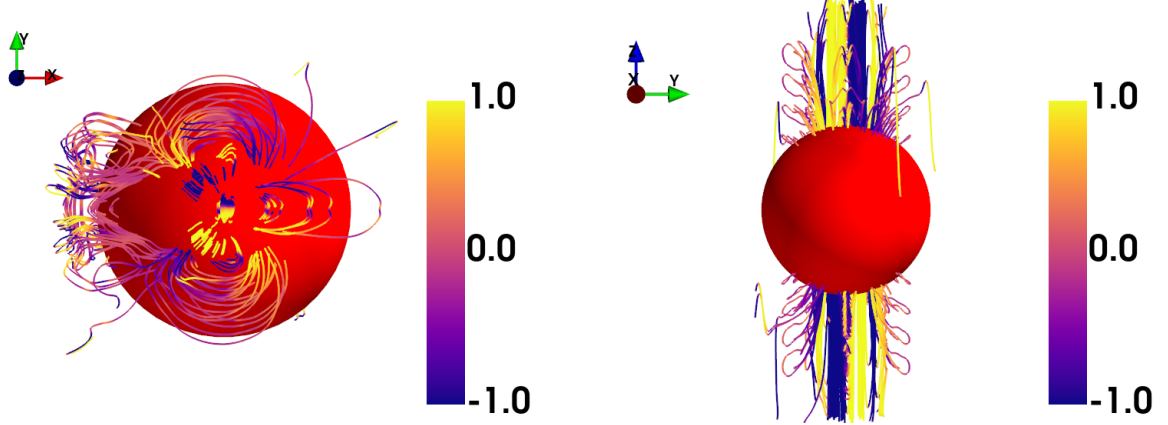


Figure 4. Non-relativistic Sub-Alfvénic run A1. We show 3D streamlines of the current colored by J_z for flow past a perfectly conducting sphere. *Left:* View along $+z$ direction. The upstream hemisphere ($x > 0$) hosts an antisymmetric pair of organized current sheets wrapping around the nose. Downstream ($x < 0$), current streamlines show lateral circulation patterns that provide closure paths connecting surface currents to the Alfvén wing channels. *Right:* View along $+x$ direction. Bipolar, field-aligned J_z structures (Alfvén wings) extend above and below the equator, with organized collimated current channels propagating downstream.

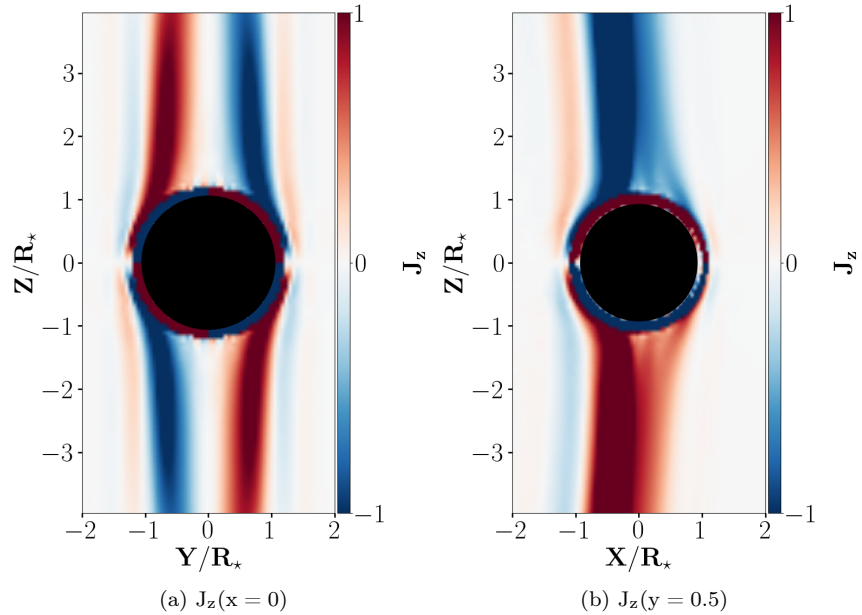


Figure 5. Non-relativistic Sub-Alfvénic run A1. Here we show 2D slices of parallel current J_z along $x = 0$, and $y = 0.5$. In the left panel, we observe currents with alternating directions, while an upstream-downstream asymmetry is clearly visible in the right image.

4.2. Moderate Sub-Alfvénic Flow

We next consider a moderately sub-Alfvénic case (run A2; $\mathcal{M}_A \approx 0.63$, $\beta \approx 0.01$), which lies in the transitional regime between coherent Alfvén wings and more compressive, asymmetric flow. In contrast to the smooth, magnetically guided structure of the strongly sub-Alfvénic case, the interaction here becomes more compressive and asymmetric. The velocity field (Fig. 6a) shows stronger deflection around the obstacle and the development of an extended downstream wake where the flow nearly stagnates. Correspondingly, the density and ram-pressure maps (Fig. 6b–c) exhibit substantial compression immediately behind the star, with peak values reaching $\rho/\rho_0 \sim 5$ and enhanced ram pressure along the equatorial flanks. These high-pressure lobes trace regions where the converging flow accumulates before being redirected into the wake.

Magnetic pressure enhancements become more localized and concentrated than in the strongly sub-Alfvénic run (Fig. 6d), indicating stronger field compression near the obstacle. Consistent with this picture, the fast magnetosonic Mach number (Fig. 6e) depicts extended super-fast regions and a wide downstream wedge. At the same time, sub-fast flow is now confined to regions near the stellar surface and portions of the upstream flow.

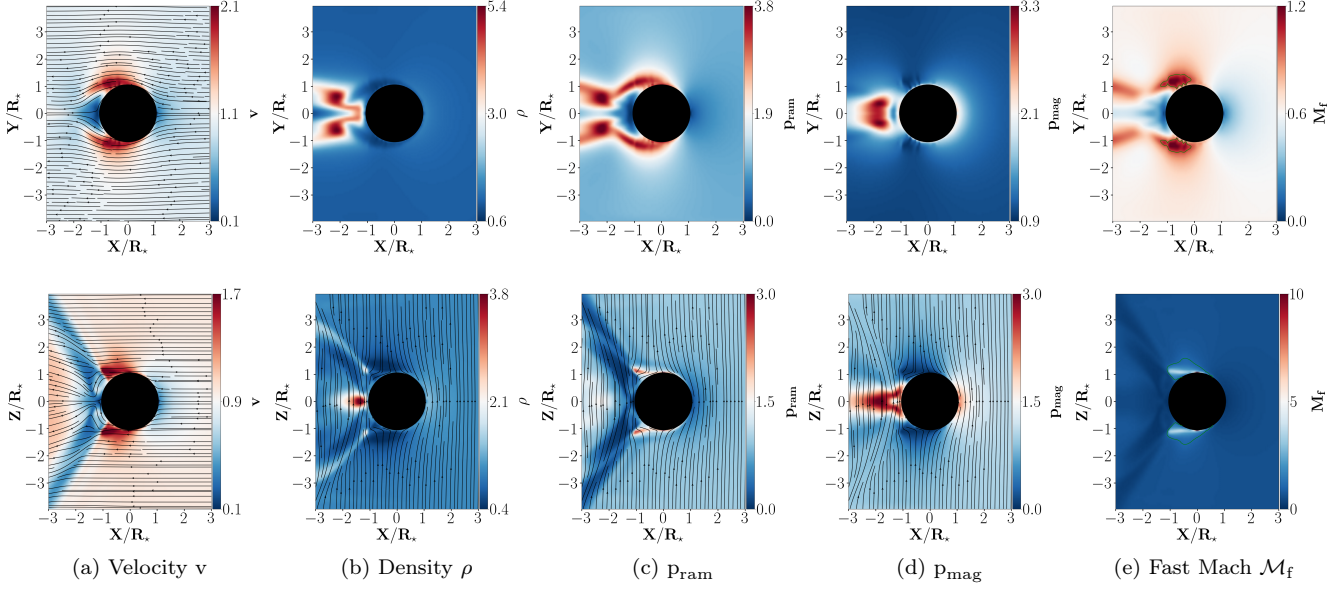


Figure 6. Moderate sub-Alfvénic run A2 ($\mathcal{M}_A \approx 2.2, \beta = 0.1$). The details are the same as in Fig. 1.

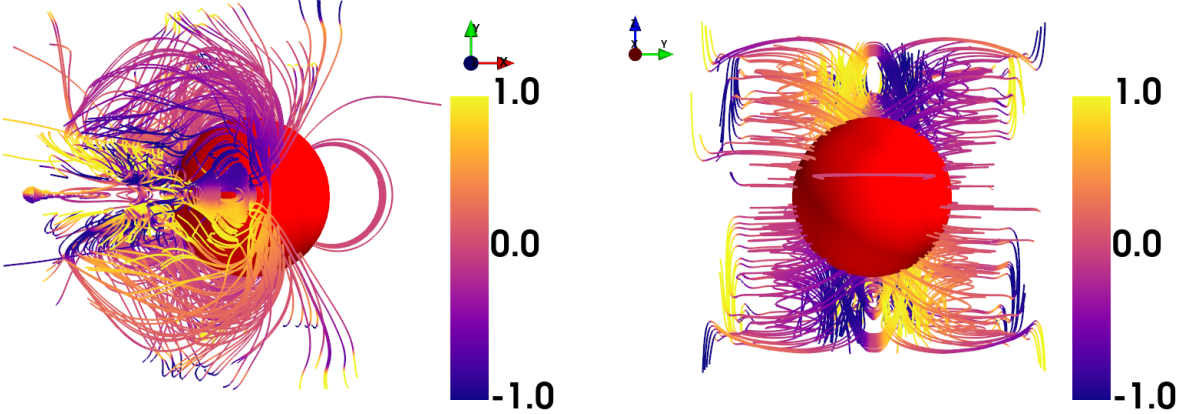


Figure 7. Moderate sub-Alfvénic run A2. 3D streamlines plot of current density at the steady state as viewed across $+z$ axis (left panel) and $+x$ axis (right panel)

Fig. 7 shows the three-dimensional current streamlines for this run. Although the current structure is more complex than in the strongly sub-Alfvénic regime (run A1), organized field-aligned patterns remain visible. Viewed along the $+x$ direction (left), current streamlines wrap around the obstacle with increased concentration in the upstream and lateral regions, while the downstream wake contains denser and more bundled current channels. Viewed along the $+z$ direction (right), a bipolar current system persists above and below the equator, indicating that the Alfvén wing geometry survives as the flow approaches the trans-Alfvénic regime. This coexistence of compressed, tangled currents with residual wing-like structure is consistent with the transitional nature of this regime.

Finally, we quantify how the field-aligned current strength depends on the upstream flow and magnetic field by measuring the integrated current in the Alfvén wings across several non-relativistic, sub-Alfvénic runs.

v_0	B_0	M_A	I_{wings}	v_0	B_0	M_A	I_{wings}
0.10	7.09	0.014	0.1031	0.80	15.85	0.05	0.6445
0.20	1.59	0.126	0.1569	1.20	15.85	0.076	0.8890
0.40	5.01	0.08	0.3208	4.20	15.85	0.26	3.0736
0.40	15.85	0.025	0.3880	10.0	15.85	0.63	9.683

Table 2. Measured wing current I_{wings} through $z = 1.5$ for various non-relativistic sub-Alfvénic runs.

To quantify this behavior, we computed the flux of field-aligned current density through transverse xy slices at fixed $z = z_0$. We first calculated the field-aligned current density $\mathbf{J}_{\parallel} = (\mathbf{J} \cdot \hat{\mathbf{b}})\hat{\mathbf{b}}$, where $\hat{\mathbf{b}}$ is the local magnetic field unit vector, and then calculated the current via $\iint \mathbf{J}_{\parallel} \cdot d\mathbf{A}$, giving us

$$\begin{aligned} I_+(z_0) &= \iint_{y>0} J_{\parallel,z}(x,y,z_0) dA \\ I_-(z_0) &= \iint_{y<0} J_{\parallel,z}(x,y,z_0) dA \end{aligned} \quad (10)$$

Due to the anti-symmetry of the current system, this magnitude is roughly the same in the other half ($y < 0$), so the total current carried by the two Alfvén wings is $I_{\text{wings}}(z_0) = |I_+(z_0)| + |I_-(z_0)|$. The wings are cleanly separated by the sign of y , reflecting the expected bipolar structure. For this calculation, we evaluated the current at $z_0 = 1.5R_*$, a distance sufficient to capture the wing structure outside the stellar surface.

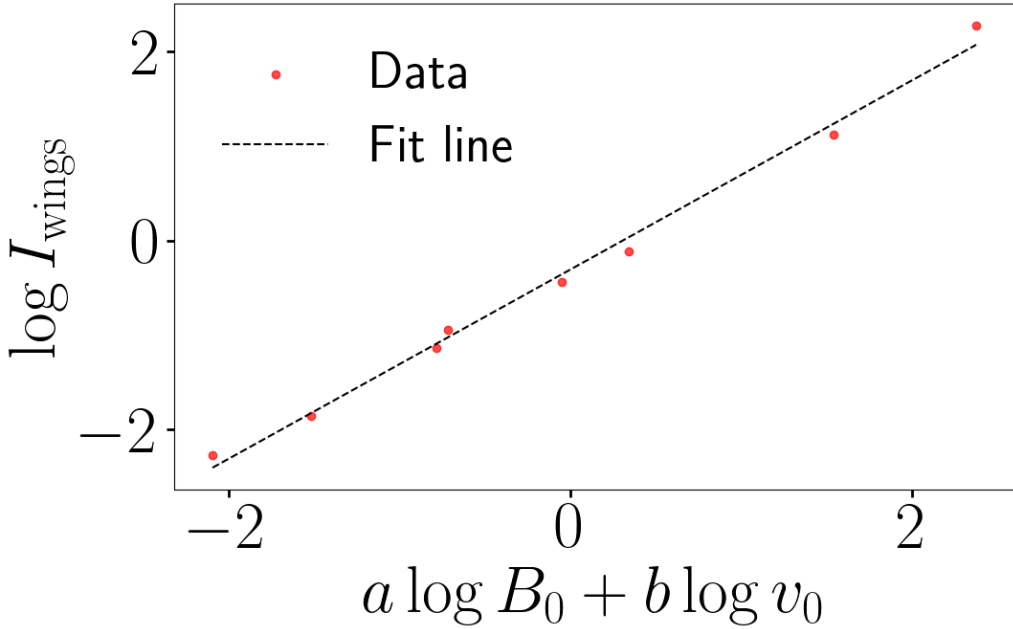


Figure 8. Scaling of the integrated field-aligned current through the $z_0 = 1.5R_*$ transverse plane (I_{wings}) as a function of the inflow velocity v_0 and background magnetic field strength B_0 . A log-log regression over selected 7 sub-Alfvénic runs (Table 2) gives $I_{\text{wings}} \propto v_0^{0.96 \pm 0.05} B_0^{0.06 \pm 0.08}$ with $R^2 \approx 0.99$. The stronger sensitivity to flow speed suggests that faster flows drive substantially larger currents.

As shown in Fig. 8, the total field-aligned current shows a power-law dependence:

$$I_{\text{wings}} \propto v_0^{0.96} B_0^{0.06} \propto M_A^{0.96} B_0^{1.02} \quad (11)$$

indicating that the current is primarily controlled by the flow speed, with only a weak dependence on B_0 . Because M_A depends on B_0 through v_A at fixed density, the apparent M_A scaling should be interpreted as an empirical fit over the explored parameter range rather than as independent scaling with M_A and B_0 .

Similar scalings arise in analytic and semi-analytic models of planetary Alfvén wing interactions (Neubauer 1980; De Colle et al. 2025; Lyutikov 2011). We would like to mention that our definition of I_{wings} refers specifically to the field-aligned current flux crossing a transverse $z = z_0$ plane. In contrast, traditional models generally consider currents integrated over the full surface of the obstacle. So variations from theory are expected. The strong sensitivity to v_0 suggests that faster flows can drive substantially larger currents. In astrophysical settings such as compact-object binaries, this trend may enhance electromagnetic energy transport during late inspiral, potentially strengthening any associated precursor emission.

4.3. Super-Alfvénic Flow

In the super-Alfvénic case (run A3; $\mathcal{M}_A > 1$), the flow exhibits a hydrodynamic-dominated interaction. Magnetic effects are largely confined to a thin boundary layer around the stellar surface, while the bulk flow forms a sharp bow shock and narrow downstream wake (Fig. 9). Density, ram-pressure, and fast magnetosonic Mach number distributions follow the expected flow-dominated pattern.

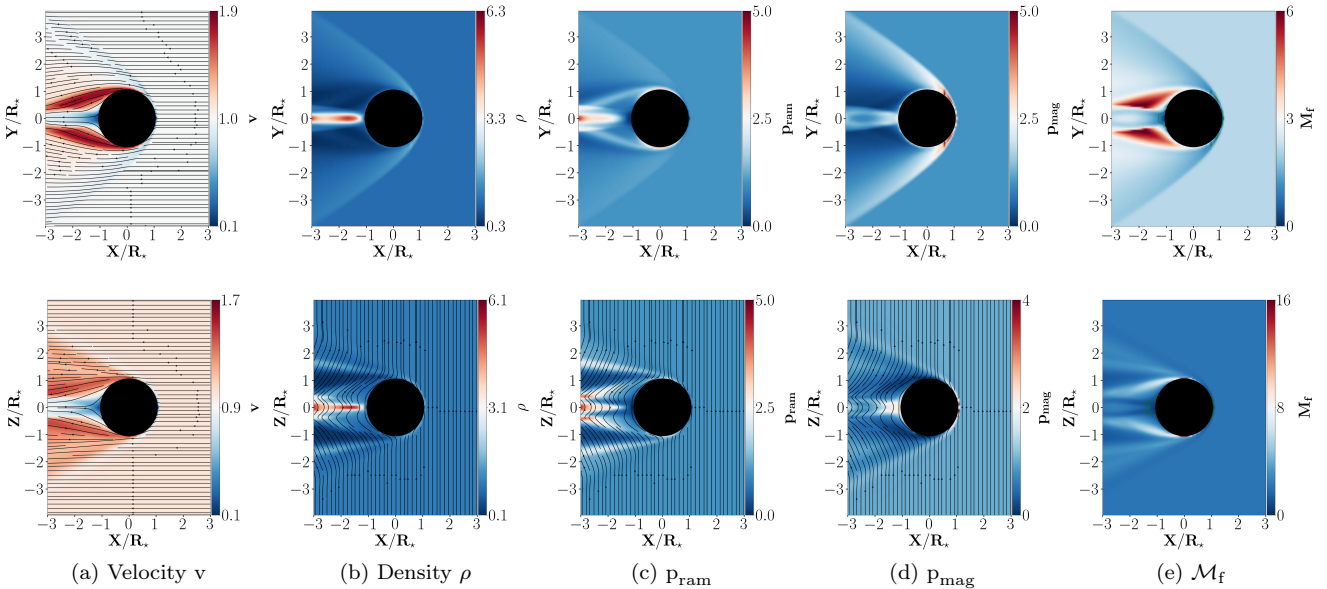


Figure 9. Super-Alfvénic run A3. The details are the same as in Fig. 1.

The 3D current structure (Fig. 10) confirms a complete breakdown of the organized Alfvén wing topology seen at lower \mathcal{M}_A . In both the $z = 0$ equatorial plane (left) and the isometric view (right), current streamlines form tangled, irregular patterns with extensive looping. The upstream flow remains laminar far from the obstacle, but becomes disrupted immediately upon encountering the bow shock and compressed boundary layer.

This regime represents a qualitative shift in the interaction physics. Whereas lower \mathcal{M}_A runs channel electromagnetic energy along well-defined current systems, the super-Alfvénic case confines magnetic structuring to the vicinity of the obstacle. This makes the regime a plausible source of strong electromagnetic emission, though the loss of coherence implies that any associated signatures should be more variable and broadband compared to the organized, wing-driven emission in the sub-Alfvénic limit.

5. RELATIVISTIC FLOW

We now extend our investigation to relativistic velocities relevant to the inspiral phase of neutron star mergers. The combination of relativistic motion and perfect conductivity fundamentally alters the interaction physics compared to both the classical MHD case and planetary analogues. We analyze the system's evolution across different plasma regimes by varying the Alfvén Mach number (\mathcal{M}_A) and plasma beta (β) parameters (see §3.3 for a complete list). Results for the sub-Alfvénic and super-Alfvénic regimes are presented separately below. All relevant quantities are evaluated in the lab frame.

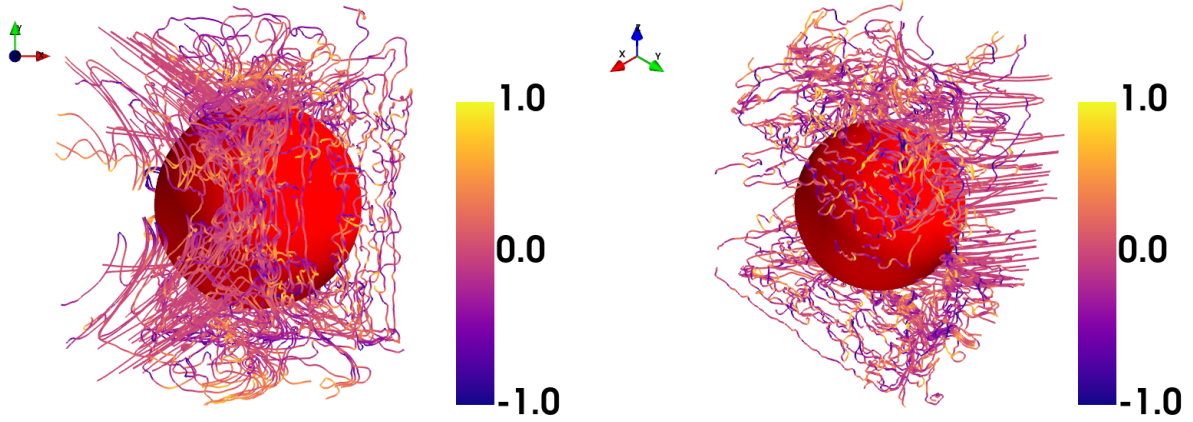


Figure 10. Super-Alfvénic run A3. 3D streamlines plot of current density at the steady state as viewed across various planes, with the viewing direction labeled in the plots.

5.1. Relativistic Sub-Alfvénic Flow

Run B1 explores the mildly relativistic strongly sub-Alfvénic regime with $v_0 = 0.30c$ (i.e., $\Gamma = 1.05$) and $\mathcal{M}_A = 0.21$ at plasma beta $\beta \approx 0.16$. This setup isolates relativistic effects while maintaining sub-Alfvénic conditions, allowing direct comparison with non-relativistic results and providing a baseline for understanding magnetic field dominance in relativistic flows.

Fig. 11(a) shows the flow velocity. In the equatorial plane, the flow undergoes smooth, symmetric deflection around the obstacle, with velocity enhancement near $y \approx \pm 1$ as plasma accelerates around the magnetosphere. In the xz plane, the flow becomes asymmetric, with preferential deflection along oblique channels aligned with the background magnetic field. The plasma density shows a localized enhancement at $(x, z) \approx (-1, 0) R_\star$, downstream of the obstacle. This enhancement extends along the equatorial plane ($z = 0$) as a narrow density ridge that gradually decays downstream as the flow advects trapped material away from the interaction region. Far from the obstacle, the density remains close to ambient values. The physical origin of this on-axis wake compression, whether due to magnetic field line convergence in the equatorial current sheet, flow re-convergence behind the obstacle, or boundary condition effects, requires further investigation. The formation of a small downstream bubble was also observed by (Corso & Lai 2025).

Ram-pressure maps show enhanced compression along the equatorial flanks, forming a double-crescent pattern, whereas the downstream wake exhibits reduced ram pressure, consistent with diversion into the Alfvén wings. Magnetic pressure is modestly amplified ($P_{\text{mag}}/P_{\text{mag},0} \sim 2 - 2.3$) in a thin shell surrounding the obstacle, forming a toroidal ring in the equatorial plane and stronger equatorial enhancement in meridional slices, while polar regions remain less affected.

The fast magnetosonic Mach number confirms that the interaction remains largely sub-unity throughout the domain. Overall, these results indicate that the magnetic field organizes the flow, producing coherent wing-like channels and localized compression, without any extended shock formation.

Fig. 12 then shows the current density. The system exhibits the characteristic Alfvén wing geometry, well-organized field-aligned channels form a bipolar structure above and below the equatorial plane, carrying oppositely directed currents along the background magnetic field. Near the obstacle, magnetic draping produces an elongated downstream current sheet, where oppositely directed components converge, and azimuthal currents flow in the equatorial plane. Color coding of the vertical current component (J_z) highlights the upward and downward flows feeding the wings, while the equatorial band shows predominantly azimuthal currents associated with the draping layer. Minor turbulent features (twisted streamlines and small loops at the outer edges) suggest weak current-driven instabilities, but the overall structure remains coherent and organized, consistent with the magnetically-dominated regime where $B^2 \gg E^2$ throughout the domain.

5.2. Moderate Sub-Alfvénic Relativistic Flow

Run B2 explores a moderately sub-Alfvénic relativistic regime with $v_0 = 0.50c$ ($\Gamma = 1.15$), $\mathcal{M}_A \approx 0.65$, and $\beta = 0.40$. This case marks the transition from magnetically dominated to kinetically dominated flow, where ram pressure begins to exceed magnetic pressure and the flow becomes increasingly compressive.

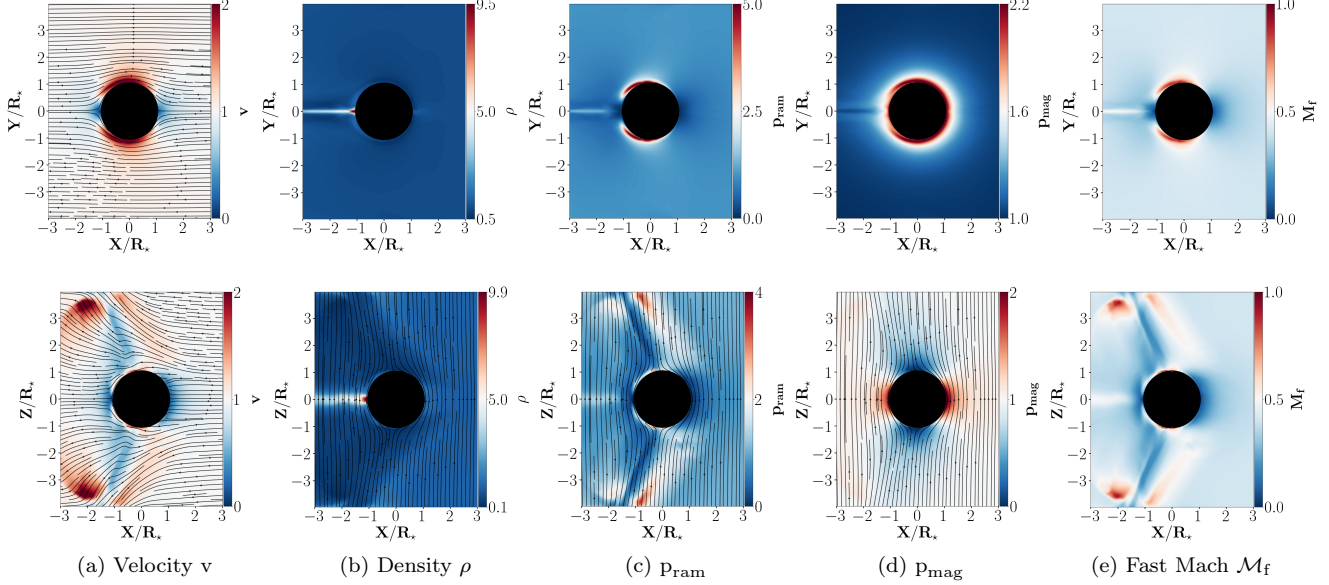


Figure 11. Relativistic Sub-Alfvénic run B1. The details are similar to those in Fig. 1. All quantities are measured in the lab frame and normalized accordingly.

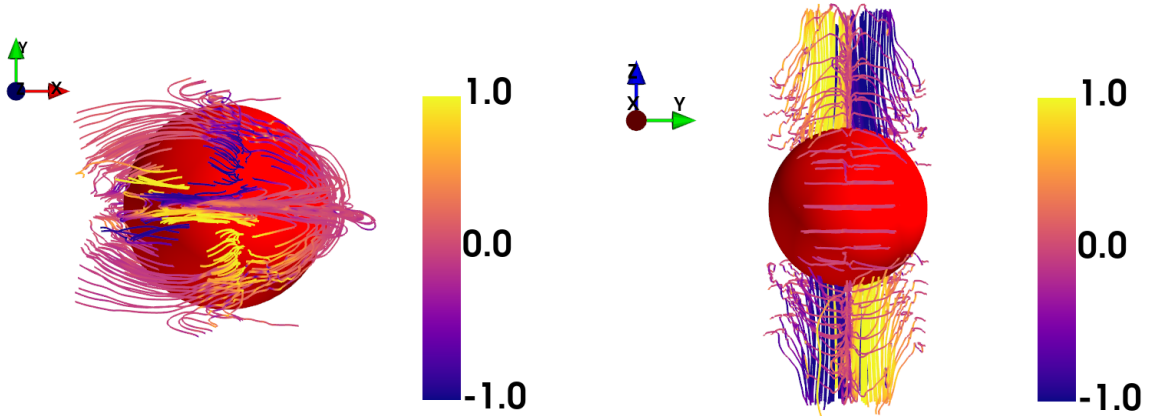


Figure 12. Relativistic Sub-Alfvénic run B1. We show 3D current density streamlines colored by J_z for relativistic flow past a conducting sphere. Left: $z = 0$ equatorial view. Right: $x = 0$ meridional view.

Compared to the smooth, strongly sub-Alfvénic flow (B1), the velocity field shows sharper gradients and pronounced deflection around the obstacle, with accelerated equatorial flanks and organized downstream channels. The density distribution reveals a patchy, partially compressed wake with a weaker downstream enhancement than in B1, indicating that magnetic confinement is still operative but less effective. Ram pressure peaks are substantially larger, concentrated along equatorial flanks and upstream regions, while the wake exhibits reduced values. Magnetic pressure remains amplified in an equatorial ring and polar lobes, but it is weaker than ram pressure, confirming kinetic dominance.

The fast magnetosonic Mach number indicates extended super-fast patches, following the trend seen earlier. Overall, this run shows a regime in which organized Alfvén -wing structures begin to fragment under the influence of strong ram pressure.

Fig. 14 shows the current structure in this run. Field-aligned channels along $\pm z$ still form a bipolar Alfvén wing system, but the streamlines are significantly disrupted as the coherent columns are replaced by twisted, tangled structures indicative of current-driven instabilities. The equatorial plane reveals a fragmented wake with multiple current channels rather than a single organized sheet, reflecting asymmetry and partial breakdown of the wing geometry.

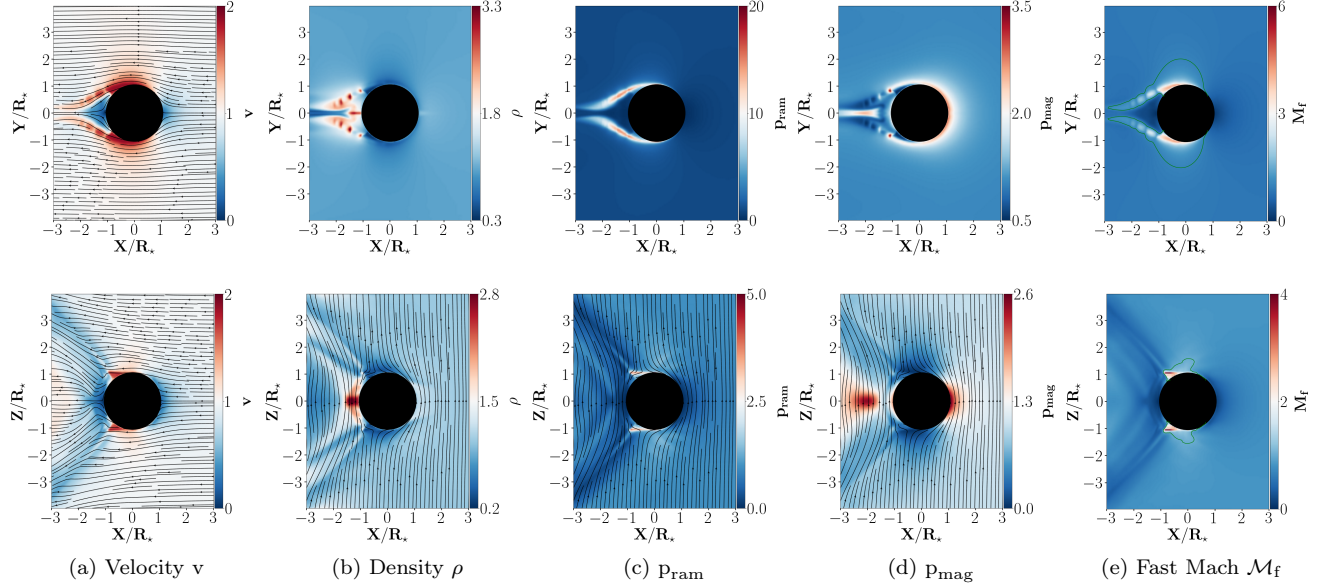


Figure 13. Relativistic moderate sub-Alfvénic run B2. Details are similar to Fig. 11.

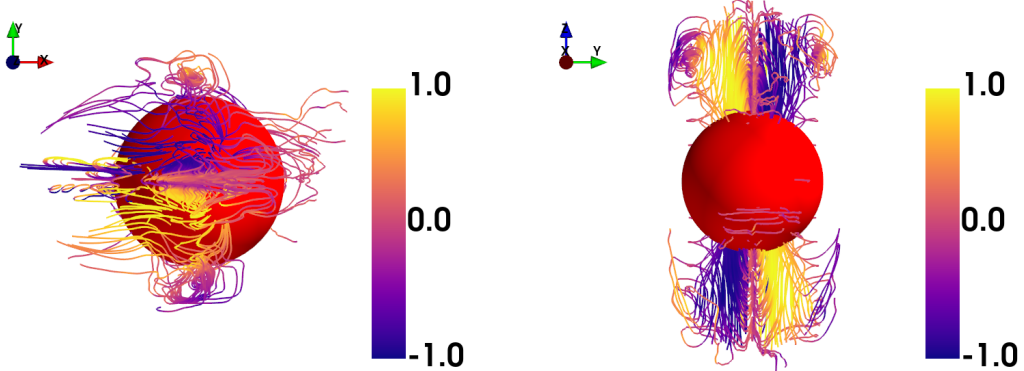


Figure 14. Moderately relativistic sub-Alfvénic run B2. 3D streamlines of current density at the steady state, viewed across various planes, with the viewing direction labeled in the plots. The rest of the details are the same as in Fig. 12.

Overall, the topology demonstrates that while Alfvén wing patterns persist, the increasing ram pressure induces instabilities and localized turbulence, signaling the transition from purely magnetically guided to more complex flow.

In the relativistic sub-Alfvénic regime, the total Alfvén wing current is expected to scale as

$$I \sim 4R_* E_0 \Sigma_A, \quad (12)$$

where $E_0 \sim v_0 B_0$ is the motional electric field and $\Sigma_A \sim \Gamma^2/v_A$ is the relativistic Alfvén conductance (Mottez & Heyvaerts 2011). Since $v_A \propto B_0$ in these runs, the dependence on B_0 largely cancels out, yielding

$$I \propto v_0 \Gamma^2. \quad (13)$$

Thus, even modest increases in Γ should lead to significantly Alfvén wing currents, consistent with the enhanced current channels observed in run B2 compared to B1.

To quantify this behavior, we computed the flux of field-aligned current using the steps discussed in the § 4.2 using Eq. 10. For comparison with analytic expectations, we extracted the values of $I_{\text{wings}}(z_0)$ across several slices. An inspection of the computed values supports the qualitative scaling predicted above. The ratio of the wing current averaged over $z_0 \in [1.5, 3.5]$ in run B2 to sub-Alfvénic run B1 is ≈ 1.8 , which is broadly consistent with the $I \propto v_0 \Gamma^2$ relationship (theoretical ratio ~ 2.0) predicted by relativistic Alfvén wing theory.

5.3. Super-Alfvénic Relativistic Flow

Lastly, we examine the trans-Alfvénic run B3, with $\mathcal{M}_A \approx 1.9$. Achieving such a high Alfvénic Mach number in a stable configuration requires a weaker magnetic field, and we therefore adopt $\beta = 0.8$, compared to $\beta = 0.4, 0.16$ in runs B1 and B2. Attempts to reach similar \mathcal{M}_A at lower β led to numerical instabilities. This setup places the system in a regime of weak electromagnetic coupling, allowing us to test whether organized magnetic draping persists when magnetic forces are subdominant.

Fig. 15 shows the relevant plots. The flow deflects smoothly around the obstacle in a largely hydrodynamic manner, without the sharp channeling or well-defined Alfvén wings seen in B1 and B2. The density distribution shows a clear bow shock with a well-defined shock cone and a broad upstream compression region. The compression is the weakest among the three cases, with $\rho_{\max} \sim 2.6$, compared to 3.54 in B2 and 10.0 in B1. Downstream, no magnetically confined bubble forms; instead, the wake is diffuse and irregular, with wavy, chaotic streamlines indicative of Alfvénic disturbances extending far from the obstacle. The ram-pressure distribution follows a similar morphology.

Magnetic pressure amplification is modest and confined to a thin upstream boundary layer; the high- β conditions ensure that magnetic forces are subdominant. Downstream, the field is diffuse and disorganized, reflecting weak coupling between the plasma and the magnetic field at high \mathcal{M}_A . Fast magnetosonic Mach numbers indicate super-fast regions along the flanks tracing ram-pressure features. Overall, this regime is governed primarily by hydrodynamic compression and flow acceleration, consistent with a shock-dominated, magnetically weak interaction.

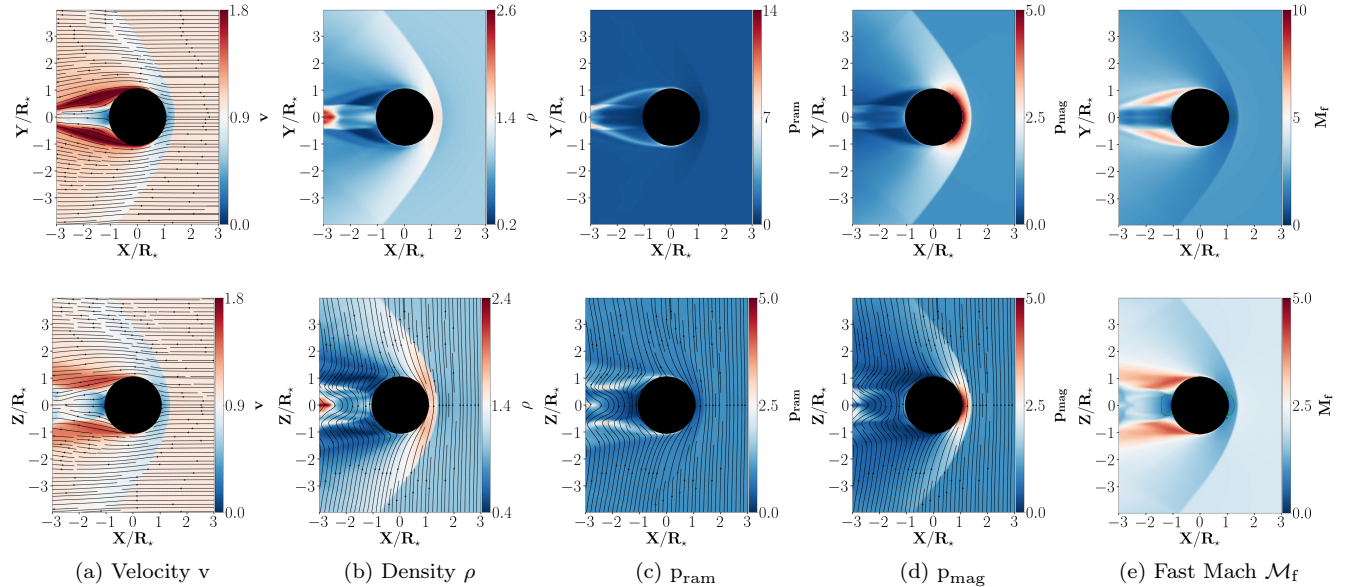


Figure 15. Relativistic trans-Alfvénic run B3. Details are similar to Fig. 11.

The current structure (Fig. 16) shows a topology distinctly different from runs B1 and B2. The coherent field-aligned Alfvén wings are absent. Instead, current streamlines form predominantly toroidal loops wrapping around the obstacle, with currents confined to the near-sphere region rather than extending along $\pm z$ to the far field. Viewed against the flow direction (left panel), the lack of organized vertical current channels contrasts sharply with B1's columnar structure and B2's turbulent wings. Streamlines exhibit primarily horizontal geometry ($J_z \approx 0$), indicating currents flow in planes perpendicular to the background magnetic field. The equatorial view (right panel) shows current concentration in the bow shock layer wrapping the upstream region, while the downstream wake remains largely current-depleted. The trans-Alfvénic flow suppresses field-aligned current propagation, confining dissipation to the immediate upstream interaction region.

6. DISCUSSION

In this work, we model the interaction of a mildly relativistic conducting body with highly magnetized plasma. We demonstrate that such velocity-driven electromagnetic interaction provides a natural and physically motivated

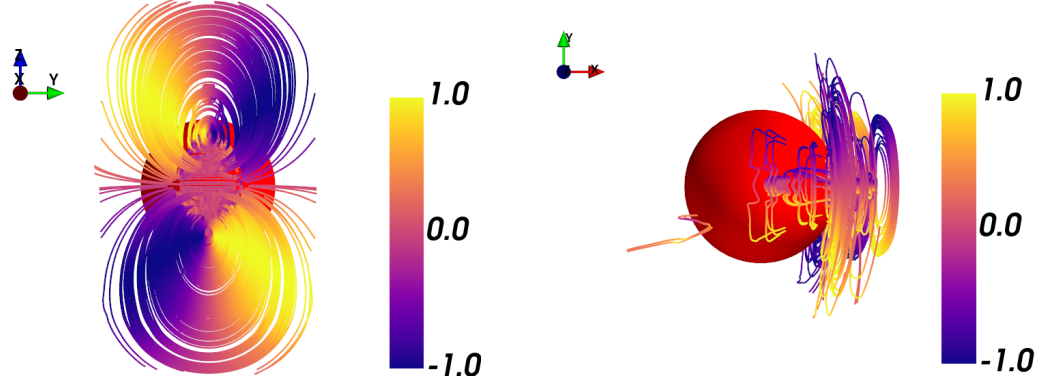


Figure 16. Relativistic super-Alfvénic run B3. 3D streamlines plot of current density at the steady state as viewed across various planes, with the viewing direction labeled in the plots. The rest of the details are the same as in Fig. 12.

framework for the generation of beamed electromagnetic emission before the neutron star merger. The electromagnetic can proceed gravitational-waves by seconds to minutes, and may be detectable (Lyutikov 2024).

Our results show that the Alfvénic Mach number \mathcal{M}_A controls the transition between coherent Alfvén wing structures and more dissipative, compressed interactions. The realistic inspiral of a neutron star binary is best represented by the relativistic B-series simulations, which suggest a clear evolutionary sequence. During the early inspiral, when the flow is sub-Alfvénic ($\mathcal{M}_A \lesssim 0.2$), coherent wings dominate the interaction. As the system evolves into the mid-to-late inspiral and approaches trans-Alfvénic conditions ($\mathcal{M}_A \sim 0.6\text{--}2$), a complex regime emerges in which distorted Alfvén wings coexist with enhanced compression and turbulence. In the final stages of inspiral, should the system reach strongly trans-Alfvénic or super-Alfvénic velocities, Alfvén wings may collapse entirely, leaving a shock-dominated interaction with strongly suppressed wing formation.

We do not address the emission mechanism *per se*. Instead, we invoke a pulsar-like paradigm of “emission follows the current”: large-scale currents would become dissipative (unstable) to the generation of both coherent radio emission and high-energy emission. A particular example of the concept “emission follows the current” is the horseshoe-like shape of the emission in PSR J0737-3039B (Figs. 5 and 7 in Lomiashvili & Lyutikov 2014), that matches the polar cap current structure (Fig. 4 in Bai & Spitkovsky 2010).

6.1. Implications for neutron star merger precursors

As neutron stars inspiral and orbital velocities increase, the interaction naturally evolves through the $B1 \rightarrow B2 \rightarrow B3$ sequence. Early inspiral exhibits stable Alfvén-wing-driven emission with strong magnetic confinement. The transitional mid-inspiral phase (B2-like, $\mathcal{M}_A \sim 0.6$), where wings become distorted and turbulent, may produce enhanced dissipation and complexity. Late inspiral (B3-like, $\mathcal{M}_A \sim 2$) becomes increasingly shock-dominated with partial suppression of large-scale electromagnetic circuits, potentially yielding different emission characteristics as the flow becomes less magnetically organized.

Finally, we note that black hole–neutron star mergers should produce Alfvén wings as well (Lyutikov 2011). Schwarzschild black holes moving through magnetized plasma act as unipolar inductors, similar to neutron stars. Though the mathematics of the corresponding effects are different in the case of neutron stars and black hole (black hole do not have a conducting surface), heuristically, the analogy can be understood in terms of the Membrane Paradigm (Thorne et al. 1986).

6.2. Limitations and future directions

Several simplifying assumptions limit the scope of this study. We model the neutron star as a perfectly conducting, unmagnetized sphere embedded in a uniform background magnetic field. While this setup captures the essential coupling between a conducting obstacle and an external magnetic field, it neglects the star’s intrinsic dipole field, internal structure, and spin. In addition, we focus exclusively on the 1M-DNS configuration. Systems in which both neutron stars are strongly magnetized (the 2M-DNS case) are expected to exhibit even stronger interactions and more complex magnetic topologies.

All simulations use ideal classical or relativistic MHD, so dissipation arises only from numerical resistivity at grid scales. We do not include explicit resistivity, radiation reaction, or kinetic plasma physics, each of which is likely

essential for resolving magnetic reconnection and converting Poynting flux into observable electromagnetic emission. Finally, the simulated flows are only mildly relativistic ($\Gamma \lesssim 1.5$) and moderately magnetized. Exploring more extreme, pulsar-wind-like regimes with higher magnetization σ will require dedicated RMHD simulations with increased resolution and tighter numerical control.

Future work should extend these calculations in several directions. Resistive RMHD or kinetic (PIC) simulations would help resolve the structure of current sheets and quantify particle acceleration more accurately, moving beyond the numerical dissipation present in ideal codes. Future observational modeling should account for both localized dissipation and extended wing transport when predicting precursor light curves and spectra.

7. ACKNOWLEDGMENTS

We would like to thank Vasily Beskin for pointing out to us the original paper on the concept of Alfvén wings (Gurevich 1962).

REFERENCES

Andrews, J. J., Breivik, K., Pankow, C., D. ÅOražio, D. J., & Safarzadeh, M. 2020, The Astrophysical Journal Letters, 892, L9, doi: [10.3847/2041-8213/ab5b9a](https://doi.org/10.3847/2041-8213/ab5b9a)

Bagenal, F., & Dols, V. 2020, Journal of Geophysical Research (Space Physics), 125, e27485, doi: [10.1029/2019JA027485](https://doi.org/10.1029/2019JA027485)

Bai, X.-N., & Spitkovsky, A. 2010, ApJ, 715, 1282, doi: [10.1088/0004-637X/715/2/1282](https://doi.org/10.1088/0004-637X/715/2/1282)

Balsara, D. S., & Kim, J. 2004, ApJ, 602, 1079, doi: [10.1086/381051](https://doi.org/10.1086/381051)

Blandford, R. D. 2002, in Lighthouses of the Universe: The Most Luminous Celestial Objects and Their Use for Cosmology, ed. M. Gilfanov, R. Sunyeav, & E. Churazov, 381, doi: [10.1007/10856495_59](https://doi.org/10.1007/10856495_59)

Caruso, A., Buccino, D., Coffin, D., et al. 2024, in European Planetary Science Congress, EPSC2024-726, doi: [10.5194/epsc2024-726](https://doi.org/10.5194/epsc2024-726)

Chané, E., Saur, J., Neubauer, F. M., Raeder, J., & Poedts, S. 2012, Journal of Geophysical Research (Space Physics), 117, A09217, doi: [10.1029/2012JA017628](https://doi.org/10.1029/2012JA017628)

Chow, A., Rowan, M. E., Sironi, L., et al. 2023, MNRAS, 524, 90, doi: [10.1093/mnras/stad1833](https://doi.org/10.1093/mnras/stad1833)

Chust, T., Roux, A., Kurth, W. S., et al. 2005, Planetary and Space Science, 53, 395, doi: [10.1016/j.pss.2004.09.021](https://doi.org/10.1016/j.pss.2004.09.021)

Clarke, J. T., Ballester, G. E., Trauger, J., et al. 1996, Science, 274, 404, doi: [10.1126/science.274.5286.404](https://doi.org/10.1126/science.274.5286.404)

Clarke, J. T., Ajello, J., Ballester, G., et al. 2002, Nature, 415, 997, doi: [10.1038/415997a](https://doi.org/10.1038/415997a)

Cooper, A. J., Gupta, O., Wadiasingh, Z., et al. 2023, MNRAS, 519, 3923, doi: [10.1093/mnras/stac3580](https://doi.org/10.1093/mnras/stac3580)

Corso, N., & Lai, D. 2025, arXiv e-prints, arXiv:2511.14932, doi: [10.48550/arXiv.2511.14932](https://doi.org/10.48550/arXiv.2511.14932)

De Colle, F., Lin, D. N. C., Chen, C., & Li, G. 2025, MNRAS, 539, 3459, doi: [10.1093/mnras/staf707](https://doi.org/10.1093/mnras/staf707)

Dedner, A., Kemm, F., Kröner, D., et al. 2002, Journal of Computational Physics, 175, 645, doi: [10.1006/jcph.2001.6961](https://doi.org/10.1006/jcph.2001.6961)

Drell, S. D., Foley, H. M., & Ruderman, M. A. 1965, PhRvL, 14, 171, doi: [10.1103/PhysRevLett.14.171](https://doi.org/10.1103/PhysRevLett.14.171)

Gedalin, M. 1993, PhRvE, 47, 4354, doi: [10.1103/PhysRevE.47.4354](https://doi.org/10.1103/PhysRevE.47.4354)

Goldreich, P., & Julian, W. H. 1969, ApJ, 157, 869, doi: [10.1086/150119](https://doi.org/10.1086/150119)

Goldreich, P., & Lynden-Bell, D. 1969, ApJ, 156, 59, doi: [10.1086/149947](https://doi.org/10.1086/149947)

Gurevich, A. V. 1962, Planet. Space Sci., 9, 321, doi: [10.1016/0032-0633\(62\)90022-3](https://doi.org/10.1016/0032-0633(62)90022-3)

Gurram, H., Shuster, J. R., Chen, L.-J., et al. 2025, Geophys. Res. Lett., 52, 2024GL111931, doi: [10.1029/2024GL111931](https://doi.org/10.1029/2024GL111931)

Hansen, B. M. S., & Lyutikov, M. 2001, MNRAS, 322, 695, doi: [10.1046/j.1365-8711.2001.04103.x](https://doi.org/10.1046/j.1365-8711.2001.04103.x)

Kivelson, M. G., Khurana, K. K., Walker, R. J., et al. 1996, Science, 273, 337, doi: [10.1126/science.273.5273.337](https://doi.org/10.1126/science.273.5273.337)

Kopp, A., & Ip, W.-H. 2002, Journal of Geophysical Research (Space Physics), 107, 1490, doi: [10.1029/2001JA005071](https://doi.org/10.1029/2001JA005071)

Lai, D. 2012, ApJL, 757, L3, doi: [10.1088/2041-8205/757/1/L3](https://doi.org/10.1088/2041-8205/757/1/L3)

Lomiashvili, D., & Lyutikov, M. 2014, MNRAS, 441, 690, doi: [10.1093/mnras/stu564](https://doi.org/10.1093/mnras/stu564)

Lyutikov, M. 2011, PhRvD, 83, 064001, doi: [10.1103/PhysRevD.83.064001](https://doi.org/10.1103/PhysRevD.83.064001)

—. 2019, MNRAS, 483, 2766, doi: [10.1093/mnras/sty3303](https://doi.org/10.1093/mnras/sty3303)

—. 2023, PhRvE, 107, 025205, doi: [10.1103/PhysRevE.107.025205](https://doi.org/10.1103/PhysRevE.107.025205)

—. 2024, arXiv e-prints, arXiv:2402.16504, doi: [10.48550/arXiv.2402.16504](https://doi.org/10.48550/arXiv.2402.16504)

Lyutikov, M., & Hadden, S. 2012, *PhRvE*, 85, 026401, doi: [10.1103/PhysRevE.85.026401](https://doi.org/10.1103/PhysRevE.85.026401)

Mahlmann, J. F., & Beloborodov, A. M. 2024, arXiv e-prints, arXiv:2412.16280, doi: [10.48550/arXiv.2412.16280](https://doi.org/10.48550/arXiv.2412.16280)

Mattia, G., Del Zanna, L., Bugli, M., et al. 2023, *A&A*, 679, A49, doi: [10.1051/0004-6361/202347126](https://doi.org/10.1051/0004-6361/202347126)

Metzger, B. D., & Berger, E. 2012, *ApJ*, 746, 48, doi: [10.1088/0004-637X/746/1/48](https://doi.org/10.1088/0004-637X/746/1/48)

Mignone, A., Bodo, G., Massaglia, S., et al. 2007, *ApJS*, 170, 228, doi: [10.1086/513316](https://doi.org/10.1086/513316)

Mignone, A., Tzeferacos, P., & Bodo, G. 2010, *Journal of Computational Physics*, 229, 5896, doi: [10.1016/j.jcp.2010.04.013](https://doi.org/10.1016/j.jcp.2010.04.013)

Mignone, A., Ugliano, M., & Bodo, G. 2009, *MNRAS*, 393, 1141, doi: [10.1111/j.1365-2966.2008.14221.x](https://doi.org/10.1111/j.1365-2966.2008.14221.x)

Most, E. R., & Philippov, A. A. 2020, *ApJL*, 893, L6, doi: [10.3847/2041-8213/ab8196](https://doi.org/10.3847/2041-8213/ab8196)

Mottez, F., & Heyvaerts, J. 2011, *A&A*, 532, A21, doi: [10.1051/0004-6361/201116530](https://doi.org/10.1051/0004-6361/201116530)

Mottez, F., & Zarka, P. 2014, *A&A*, 569, A86, doi: [10.1051/0004-6361/201424104](https://doi.org/10.1051/0004-6361/201424104)

Neubauer, F. M. 1980, *J. Geophys. Res.*, 85, 1171, doi: [10.1029/JA085iA03p01171](https://doi.org/10.1029/JA085iA03p01171)

—. 1999, *J. Geophys. Res.*, 104, 28671, doi: [10.1029/1999JA900217](https://doi.org/10.1029/1999JA900217)

Portegies Zwart, S. F., & Spreeuw, H. N. 1996, *A&A*, 312, 670

Powell, K. G. 1994, Approximate Riemann solver for magnetohydrodynamics (that works in more than one dimension)

Powell, K. G., Roe, P. L., Linde, T. J., Gombosi, T. I., & De Zeeuw, D. L. 1999, *Journal of Computational Physics*, 154, 284, doi: [10.1006/jcph.1999.6299](https://doi.org/10.1006/jcph.1999.6299)

Pshirkov, M. S., & Postnov, K. A. 2010, *Ap&SS*, 330, 13, doi: [10.1007/s10509-010-0395-x](https://doi.org/10.1007/s10509-010-0395-x)

Saur, J., Grambusch, T., Duling, S., Neubauer, F. M., & Simon, S. 2013, *A&A*, 552, A119, doi: [10.1051/0004-6361/201118179](https://doi.org/10.1051/0004-6361/201118179)

Thorne, K. S., Price, R. H., & MacDonald, D. A. 1986, *Black holes: The membrane paradigm (Black Holes: The Membrane Paradigm)*

Tian, J., Anderson, G. E., Cooper, A. J., et al. 2023, *PASA*, 40, e050, doi: [10.1017/pasa.2023.49](https://doi.org/10.1017/pasa.2023.49)

Vernisse, Y., Riousset, J. A., Motschmann, U., & Glassmeier, K. H. 2017, *Planet. Space Sci.*, 137, 40, doi: [10.1016/j.pss.2016.08.012](https://doi.org/10.1016/j.pss.2016.08.012)

Zanotti, O., Fambri, F., & Dumbser, M. 2015, *MNRAS*, 452, 3010, doi: [10.1093/mnras/stv1510](https://doi.org/10.1093/mnras/stv1510)

Zhang, H., Khurana, K. K., Kivelson, M. G., et al. 2016, *Journal of Geophysical Research (Space Physics)*, 121, 10,698, doi: [10.1002/2016JA022360](https://doi.org/10.1002/2016JA022360)

APPENDIX

A. SIMULATION SETUP

We model the obstacle as a dense, non-rotating, perfectly conducting sphere of radius R_\star embedded in an ambient magnetized plasma. The sphere is assumed to be unmagnetized and highly conducting, and interacts with the magnetic field of a companion star.

A.1. Initial Conditions

Because the interaction occurs primarily at the interface between the star and the ambient plasma, it is sufficient to model the object as a uniform conducting sphere without internal structure. The density profile is initialized as

$$\rho = \begin{cases} \rho_\star, & r \leq R_\star, \\ \rho_{\text{amb}}, & r > R_\star. \end{cases} \quad (\text{A1})$$

and the system is initialized in pressure equilibrium with $p = p_0$.

In code units, $\rho_{\text{amb}} = p_{\text{amb}} = 1$ and $p_\star = p_{\text{amb}}$. The obstacle density is $\rho_\star = 500$ and the stellar radius $R_\star = 1$.

We work in the star's rest frame so that the neutron star remains fixed in space. Far from the sphere ($r \gg R_\star$), the plasma flows with velocity $\mathbf{v} = -v_0 \hat{\mathbf{x}}$ from right (upstream) to left (downstream). We initialize the velocity field following Eq. B4 of [Lyutikov \(2023\)](#):

$$\begin{aligned} \mathbf{v} &= 0 & r \leq R_\star \\ v_r &= -v_0 \left(1 - \frac{R_\star^3}{r^3}\right) \sin \theta \cos \varphi & r > R_\star \\ v_\theta &= -v_0 \left(1 + \frac{R_\star^3}{2r^3}\right) \cos \theta \cos \varphi & r > R_\star \\ v_\varphi &= v_0 \left(1 + \frac{R_\star^3}{r^3}\right) \sin \varphi & r > R_\star \end{aligned} \quad (\text{A2})$$

The external magnetic field of the companion is approximated as a uniform field of magnitude B_0 along the z -axis, valid when the stellar radius is much smaller than the orbital separation. The neutron star, being perfectly conducting, excludes magnetic flux through its surface. Thus, the total field is the sum of the uniform and induced components (see Eq. 16 of [Lyutikov \(2023\)](#))

$$\begin{aligned} \mathbf{B} &= 0 & r \leq R_\star \\ B_r &= B_0 \left(1 - \frac{R_\star^3}{r^3}\right) \cos \theta & r > R_\star \\ B_\theta &= -B_0 \left(1 + \frac{R_\star^3}{2r^3}\right) \sin \theta & r > R_\star \\ B_\varphi &= 0 & r > R_\star \end{aligned} \quad (\text{A3})$$

A.2. Boundary Conditions

In Cartesian runs, we fix the upstream ($x = +4R_\star$) boundary to maintain the inflow velocity $\mathbf{v} = -v_0 \hat{\mathbf{x}}$ and uniform ambient state. The downstream ($x = -4R_\star$) boundary adopts outflow conditions to allow plasma and magnetic structures to exit the domain without reflection. Lateral boundaries in y ($y = \pm 4R_\star$) and along the magnetic-field direction z ($z = \pm 4R_\star$) are also set to fixed inflow to preserve the ambient medium, preventing artificial depletion or accumulation of plasma. A subset of simulations was repeated in spherical geometry to verify coordinate independence.

Because Alfvén wings extend along the magnetic-field direction ($\pm z$), we verified that our results are not significantly affected by the finite domain size. To test for boundary effects, we repeated the relativistic sub-Alfvénic run B1 with an extended vertical domain $z \in [-8, 8]R_\star$ while keeping all other parameters identical. The integrated current flux through the transverse plane at $z = 1.5R_\star$ differed by approximately 10% between the standard and extended domains.

Since the extended domain has twice the grid spacing in the comparison region (mean $\Delta x \approx 0.09$ versus 0.05), we attribute this difference to resolution effects rather than boundary truncation. The qualitative current topology and wing structure remained consistent between both runs, confirming that the standard domain $[-4, 4]^3$ adequately captures the relevant wing dynamics without significant boundary artifacts.

A.3. Numerical Convergence

To verify the robustness of our results, we performed a convergence study for run B1 across four resolutions: $N = 113^3, 140^3, 170^3$ (fiducial), and 190^3 . As shown in Table 3, the maximum magnetic field amplification (B_{\max}/B_0) shows excellent stability, varying by less than 1% across all resolutions, indicating that the global magnetic topology is well-resolved even at the coarsest grid. The volume-integrated wing current (I_{wings}) and peak velocity (v_{\max}/v_0) exhibit stronger resolution dependence at coarse grids but show rapid convergence: relative changes compared to the fiducial resolution decrease from -3.2% ($N=113$) to only $+1.6\%$ ($N=190$) for velocity, signaling that the 170^3 grid has reached the asymptotic regime and effectively captures the essential physics.

Resolution (N^3)	v_{\max}/v_0 ($\Delta\%$)	B_{\max}/B_0 ($\Delta\%$)	I_{wings} ($\Delta\%$)
113	-3.2%	-0.7%	-10.7%
140	-7.1%	-0.5%	-5.1%
170 (Fiducial)	—	—	—
190	$+1.6\%$	$+0.7\%$	$+3.4\%$

Table 3. Convergence study for run B1. Values show relative percentage change compared to the fiducial 170^3 resolution at $t = 60$. The stabilization of all quantities at high resolution indicates the solution has converged.

A.4. Divergence Control

The divergence-free constraint $\nabla \cdot \mathbf{B} = 0$ is enforced differently for relativistic and non-relativistic runs. For the relativistic B-series, we employ the hyperbolic divergence cleaning method (Dedner et al. 2002; Mignone et al. 2010), which introduces a generalized Lagrange multiplier (GLM) coupled to the induction equation. This approach treats divergence errors as waves that propagate out of the computational domain at a characteristic speed.

For the non-relativistic A-series, we use PLUTO’s eight-wave formulation (Powell 1994; Powell et al. 1999; Balsara & Kim 2004), which adds source terms to the standard MHD equations that locally damp divergence errors. In this method, $\nabla \cdot \mathbf{B}$ is treated as an eighth non-physical wave that advects through the grid.

We monitor the volume-averaged normalized divergence error $\Delta x \langle |\nabla \cdot \mathbf{B}| \rangle / \langle |\mathbf{B}| \rangle$, where Δx is the characteristic cell spacing. As shown in Table 4, divergence errors remain below $\text{sim}10^{-3}$ for all runs, demonstrating good constraint enforcement with negligible impact on the magnetic field evolution.

Run	Resolution (N^3)	Method	Normalized Div. Error
A1	120	Eight-Wave	1.8×10^{-3}
A2	120	Eight-Wave	2.6×10^{-3}
A3	120	Eight-Wave	3.3×10^{-3}
B1	170	Hyp. Div. Clean.	4.4×10^{-4}
B2	170	Hyp. Div. Clean.	6.4×10^{-4}
B3	170	Hyp. Div. Clean.	1.2×10^{-3}

Table 4. Volume-averaged normalized divergence errors for all runs, demonstrating robust constraint enforcement.

B. PLUTO CODE

We perform both non-relativistic and relativistic MHD simulations using the PLUTO code (Mignone et al. 2007). The system evolves an ideal, perfectly conducting plasma, with numerical dissipation arising solely from finite resolution.

B.1. Non-relativistic MHD Module

The non-relativistic simulations solve the standard ideal-MHD equations with adiabatic index $\gamma = 5/3$:

$$\frac{\partial \rho}{\partial t} + \nabla \cdot (\rho \mathbf{v}) = 0, \quad (\text{B4})$$

$$\frac{\partial(\rho \mathbf{v})}{\partial t} + \nabla \cdot \left[\rho \mathbf{v} \mathbf{v} + \left(p + \frac{B^2}{2} \right) \mathbf{I} - \mathbf{B} \mathbf{B} \right] = 0, \quad (\text{B5})$$

$$\frac{\partial e}{\partial t} + \nabla \cdot \left[(e + p_t) \mathbf{v} - (\mathbf{v} \cdot \mathbf{B}) \mathbf{B} \right] = 0, \quad (\text{B6})$$

with total pressure $p_t = p + B^2/2$ and total energy

$$e = \frac{p}{\gamma - 1} + \frac{1}{2} \rho v^2 + \frac{1}{2} B^2.$$

Numerical integration employs a second-order Runge-Kutta (RK2) time-stepping scheme with CFL number 0.4, HLL Riemann solver, and the eight-wave method to enforce $\nabla \cdot \mathbf{B} = 0$. The computational domain is Cartesian, $[-4, 4]^3$, with a stretched grid of $N_x = N_y = N_z = 120$ cells, providing enhanced resolution near the stellar surface.

B.2. Relativistic MHD Module

Relativistic simulations use the special-relativistic MHD (RMHD) module, evolving

$$(D, \mathbf{m}, E_t, \mathbf{B}), \quad D = \Gamma \rho$$

according to

$$\frac{\partial}{\partial t} \begin{pmatrix} D \\ \mathbf{m} \\ E_t \\ \mathbf{B} \end{pmatrix} + \nabla \cdot \begin{pmatrix} D \mathbf{v} \\ w_t \Gamma^2 \mathbf{v} \mathbf{v} - \mathbf{b} \mathbf{b} + p_t \mathbf{I} \\ \mathbf{m} \\ \mathbf{v} \mathbf{B} - \mathbf{B} \mathbf{v} \end{pmatrix}^T = 0. \quad (\text{B7})$$

Here $\Gamma = (1 - v^2/c^2)^{-1/2}$ is the Lorentz factor, and

$$\begin{aligned} b^0 &= \Gamma \mathbf{v} \cdot \mathbf{B}, & \mathbf{b} &= \frac{\mathbf{B}}{\Gamma} + \Gamma(\mathbf{v} \cdot \mathbf{B}) \mathbf{v}, \\ w_t &= \rho h + \frac{B^2}{\Gamma^2} + (\mathbf{v} \cdot \mathbf{B})^2, & p_t &= p + \frac{1}{2} \left(\frac{B^2}{\Gamma^2} + (\mathbf{v} \cdot \mathbf{B})^2 \right), \\ E_t &= w_t \Gamma^2 - (b^0)^2 - p_t, & \mathbf{m} &= w_t \Gamma^2 \mathbf{v} - b^0 \mathbf{b}. \end{aligned}$$

Integration uses RK2 time-stepping, HLLD Riemann solver, CFL = 0.25, and hyperbolic divergence cleaning to maintain $\nabla \cdot \mathbf{B} \lesssim 10^{-3}$. The computational grid spans $[-4, 4]^3$ with $N_x = N_y = N_z = 170$, and $\gamma = 4/3$.

B.3. Unit Conversion

Most simulations were performed in Cartesian coordinates, centered on the star. The upstream flow is along the $-x$ direction and the magnetic field along $+z$. Simulation quantities are expressed in dimensionless code units, with characteristic scales \tilde{L} , $\tilde{\rho}$, and \tilde{v} defining the derived units $\tilde{t} = \tilde{L}/\tilde{v}$, $\tilde{p} = \tilde{\rho}\tilde{v}^2$, and $\tilde{B} = \sqrt{4\pi\tilde{\rho}\tilde{v}^2}$. The reference values in physical (cgs) units are $\tilde{\rho} = 1.67 \times 10^{-23} \text{ g cm}^{-3}$, $\tilde{L} = 3.1 \times 10^{16} \text{ cm}$, and $\tilde{v} = 10^5 \text{ cm s}^{-1}$ (or $\tilde{v} = 3 \times 10^{10} \text{ cm s}^{-1}$ for relativistic runs).